Journal of the Indian Chemical Society 102 (2025) 102193

Contents lists available at ScienceDirect

Journal of the Indian Chemical Society

journal homepage: www.journals.elsevier.com/journal-of-the-indian-chemical-society

Facile Phyto fabrication of Mg interconnected ZrO_2 nanocomposites for effective decontamination of infected water bodies

M. Pushpa [a,*], S. Mageswari [b,**], S. Na Shereenaa [c], S. Surendhiran [d]

[a] Department of Physics, Vivekanandha College of Engineering for Women, Elayampalayam, Tiruchengode, 637205, Tamil Nadu, India
[b] Department of Chemistry, Vivekanandha College of Engineering for Women, Elayampalayam, Tiruchengode, 637205, Tamil Nadu, India
[c] Department of Physics, Swamy Vivekanandha Physiotherapy College, Elayampalayam, Tiruchengode, 637205, Tamil Nadu, India
[d] Centre for Nanoscience and Technology, K.S. Rangasamy College of Technology, Tiruchengode, Namakkal (Dt.), 637 215, Tamil Nadu, India

ARTICLE INFO

Keywords:
Green synthesis
Zirconium oxide
Mg doping
Photocatalytic
Dye degradation
Bacterial activity

ABSTRACT

This study uses Eucalyptus leaf extract to present a green synthesis approach for pristine and magnesium-doped zirconium oxide (Z and ZM) nanocomposites. The synthesis was performed with varying doping concentrations (1 %, 3 %, and 5 %) and characterized using advanced techniques. The XRD analysis confirmed the crystalline nature, with peaks corresponding to the monoclinic phase of ZrO_2 and the cubic phase of MgO. Notably, Mg incorporation reduces the crystallite size from 32.27 nm (Z) to 11.8 nm (ZM3). FE-SEM analysis revealed uniformly distributed quasi-spherical particles with smooth surfaces. At higher doping levels, particles elongated, indicating significant structural changes and stronger interparticle forces. FT-IR and EDX analysis confirmed the presence of Zr, Mg, and O elements. The UV–Vis spectra revealed that Mg doping in ZrO_2 resulted in redshifts of the absorbance peaks, accompanied by a decreasing bandgap of 2.8eV for higher concentrations (ZM3). Under 100 min solar irradiation, ZM3 achieves the highest photocatalysis of 95.43 % with $k = 0.027\ min^{-1}$ for Rhodamine B (RhB), and 97.08 % with $k = 0.03\ min^{-1}$ for Brilliant Blue (BB). ZM3 also exhibits superior cycling stability, retaining 90.3 and 92.1 % efficiency after five consecutive runs. Antibacterial activity demonstrated that ZM3 exhibited the highest zones of inhibition at 100 μg/mL, measuring 19.2 mm against *S. aureus* and 18.3 mm against *E. coli*. The performance gains are attributed to Mg-induced oxygen vacancies and defect states that enhance charge separation, suppress e^-/h^+ recombination, and increase ROS generation. The study highlights the potential of phyto-fabricated Mg-doped ZrO_2 nanocomposites as a sustainable, reusable photocatalyst for applications in wastewater treatment and antimicrobial applications.

1. Introduction

Water pollution is one of our most pressing global challenges, with its effects threatening ecosystems, public health, and sustainable development. The contamination of water sources by industrial discharges, agricultural runoff, and domestic waste has led to a growing demand for advanced water treatment solutions. While conventional treatment methods (coagulation–flocculation, filtration, chlorination, reverse osmosis) struggle with persistent dyes and emerging pathogens, and may entail high energy or secondary pollution [1–3]. Researchers have turned to nanotechnology to address these limitations, which offers innovative and efficient ways to tackle water contamination. Nanostructured metal oxides provide a route to solar-assisted advanced oxidation with reusable catalysts. Zirconium oxide nanoparticles (ZrO_2 NPs) have shown significant promise among various nanomaterials explored due to their unique physicochemical properties [4,5].

ZrO_2 NPs are renowned for their exceptional thermal stability, mechanical strength, and catalytic properties. These attributes make them highly effective in eliminating many water toxins, including heavy metals, organic pollutants, and pathogens. However, synthesizing these nanocomposites is vital in determining their properties, performance, and environmental impact [6,7]. Traditional chemical synthesis methods often involve toxic reagents and energy-intensive processes, raising concerns about their sustainability. This has driven the exploration of green synthesis approaches, which utilize natural, eco-friendly reducing agents derived from plant extracts or other biological sources.

* Corresponding author.
** Corresponding author.
E-mail addresses: pushparavip6@gmail.com (M. Pushpa), mmahes15@gmail.com (S. Mageswari).

https://doi.org/10.1016/j.jics.2025.102193
Received 14 July 2025; Received in revised form 2 October 2025; Accepted 12 October 2025
Available online 17 October 2025
0019-4522/© 2025 Indian Chemical Society. Published by Elsevier B.V. All rights are reserved, including those for text and data mining, AI training, and similar technologies.

Plant extracts are particularly popular in green synthesis due to their abundance of phytochemicals, such as alkaloids, flavonoids, and polyphenols. These compounds facilitate the reduction of metal precursors to nanoparticles while also ensuring stability and uniformity in particle size [8–10].

Additionally, plant-assisted synthesis provides benign reducers/capping agents (polyphenols, flavonoids, terpenoids) that stabilize nuclei, regulate growth, and reduce hazardous reagents. Recent surveys have shown that Eucalyptus globulus extracts have been successfully used to phyto-fabricate diverse nanoparticles, including ZrO_2, MgO, TiO_2, ZnO, and CuO, with demonstrated photocatalytic and antibacterial functions, highlighting the scalability and low-toxicity processing. This evidence supports our choice of Eucalyptus as a renewable, widely available phytochemical source to produce Mg-doped ZrO_2 with the required surface chemistry for dye degradation and pathogen control. Moreover, the widespread availability of *Eucalyptus* leaf ensures that the synthesis process remains cost-efficient and scalable for large-scale applications [11–13].

In advanced water treatment, solar and visible-light photocatalysis enhances adsorption and membrane processes by degrading organic compounds, rather than merely transferring them, and is applicable in dispersed conditions. A phytochemical approach reduces synthesis risks and facilitates scalability, whereas Mg-induced lattice defects (oxygen vacancies) and band-edge tuning enhance sunlight absorption and durability during repeated utilization. The selected materials and test dyes correspond with such goals and are compatible with realistic aqueous matrices [14,15]. Additionally, the functional performance of zirconia nanoparticles can be further enhanced through doping. This study explores the integration of green synthesis methods with the production of Mg-doped zirconia nanoparticles, aiming to develop a sustainable and efficient solution for advanced water treatment. Mg doping introduces defects in the zirconia lattice, which can enhance its catalytic activity by providing more active sites for chemical reactions. These defects also improve the material's light absorption properties, enabling the utilization of a broader spectrum of light in photocatalytic processes [16–18].

The simultaneous antibacterial action is ecologically significant as it reduces dependence on residual disinfectants and their byproducts, while also decreasing biofouling on catalyst surfaces and subsequent membranes. Exhibiting efficacy against Gram-positive (*Staphylococcus aureus*) and Gram-negative (*Escherichia coli*) bacteria indicates extensive applicability for therapeutic regimens addressing mixed microbial infections. Mg doping in our work enhances carrier separation and ROS formation, providing preliminary research for dual dye degradation and antibacterial function, which is desirable in current water-quality applications [19,20]. Although widely used photocatalysts such as TiO_2, ZnO, and g-C_3N_4 deliver good activity, ZrO_2 offers a distinctive combination of chemical/thermal stability, photocorrosion resistance, and tunable defect chemistry (oxygen vacancies) that can be engineered by aliovalent doping to improve visible-light harvesting and charge separation [21–24]. Recent reviews summarize how defect/vacancy engineering, heterojunctions, and cation/anion doping significantly enhance the photo efficacy of ZrO_2 for wastewater treatment, positioning it as a robust platform when long-term reusability is critical. In particular, oxygen-vacancy formation narrows the effective bandgap and amplifies visible-light absorption, a strategy validated in current ZrO_2 research.

Parvathiraja Chelliah et al. (2023) synthesized ZrO_2 NPs using *Murraya koenigii* leaf extract with their spherical morphology, monoclinic structure, and wide bandgap (4.7 eV). They demonstrated significant degradation of MB dye (94 % within 20 min) and potent antibacterial activity against *E. coli* and *S. aureus*. Moreover, they highlight the potential of bio-mediated ZrO_2 NPs for applications in antimicrobial development, environmental remediation, and wastewater treatment, reinforcing the viability of green synthesis as a superior alternative to chemical methods [25]. Nitha et al. (2025) green-synthesized ZnO/MgO nanocomposites (1:1 and 1:2 ratios) exhibited well-defined heterostructures, porous flake-like morphologies, and band gaps of 3.14 and 3.27 eV, respectively. The 1:1 composite exhibited superior photocatalytic degradation of the crystal violet dye (99.72 % within 75 min, $k = 0.07\ min^{-1}$) compared to the 1:2 composite (97.04 %, $k = 0.05\ min^{-1}$). Both materials demonstrated stability over four cycles, exhibited vigorous antioxidant activity (82 % inhibition), and showed anticancer potential (IC_{50} = 58.52 and 65.74 μg/mL), supporting the literature on eco-friendly multifunctional nanomaterials [26]. Abdul Muhaymin et al. (2024) presented the green synthesis of MgO NPs using *Hyphaene thebaica* fruit extract, demonstrating an environmentally friendly and cost-effective approach. Characterization techniques confirmed the cubic crystalline structure, quasi-spherical morphology, and presence of Mg–O bonds. The MgO NPs exhibited notable photocatalytic efficiency, achieving 98 % degradation of the MB dye under visible light within 110 min, highlighting their potential for environmental remediation [27].

To our knowledge, the synthesis of Mg-doped ZrO_2 using *Eucalyptus* leaf extract has not yet been reported. Phyto-fabrication of Mg-doped ZrO_2 using *Eucalyptus* leaf extract, then links the resulting defect chemistry to dual sunlight photocatalysis and antibacterial performance. The present work aims to develop a green, scalable phyto-fabrication of pristine and Mg-doped ZrO_2 using *Eucalyptus* leaf extract with tunable Mg doping and elucidate structure-property relations by comprehensive characterization and further quantify sunlight-driven photocatalytic degradation of two charge-opposite model dyes, Rhodamine B (cationic) and Brilliant Blue (anionic), using UV–Vis monitoring and pseudo-first-order kinetics. Moreover, cycling stability and reusability over five consecutive runs were assessed, and the antibacterial efficacy against *S. aureus* and *E. coli* was evaluated to establish a dual-function platform for advanced wastewater treatment.

2. Experimental details

2.1. Materials

Eucalyptus Leaves, zirconium oxychloride ($ZrOCl_2{\cdot}8H_2O$, ≥99 %, CAS No. 13520-92-8), as the source of zirconia, and magnesium nitrate hexahydrate ($Mg(NO_3)_2{\cdot}6H_2O$, ≥99 %, CAS No. 13446-18-9) are used as the doping materials. Deionized Water and Ethanol (99 %, CAS No. 64-17-5) as a solvent. Anionic Brilliant blue (BB) dye ($C_{37}H_{34}N_2Na_2O_9S_3$, CAS No. 3844-45-9) and cationic Rhodamine B (RhB) dye ($C_{28}H_{31}ClN_2O_3$, CAS No. 81-88-9) are used. Diphenyl-trinitrophenyl imino azanium (CAS No. 1898-66-4), Nutrient broth, Muller Hinton agar, Whatman filter paper, Streptomycin antibiotic (CAS No. 3810-74-0), *Staphylococcus aureus* (ATCC 25923), and *Escherichia coli* (ATCC 25922) bacterial cultures.

2.2. Leaf extract preparation

Collect the leaves, wash them thoroughly with distilled water to remove dirt, dust, and any surface contaminants, and then dry them under shade for 2–3 days to reduce their moisture content. Further, grind the dried leaves into a coarse powder. Add 10 g of powder to a beaker containing 100 mL of distilled water. Heat at 80 °C for 30 min, stirring occasionally to ensure even extraction. Then, the extract is filtered using filter paper to separate the solid residues from the liquid extract. Collect the clear filtrate, which contains the bioactive compounds, and store it in a clean, airtight container [28,29].

2.3. Nanoparticle synthesis

Dissolve 0.1 M zirconium oxychloride in 100 mL of deionized water under continuous stirring, and slowly add the *Eucalyptus* leaf extract dropwise to the zirconium solution. A color change or the formation of a cloudy precipitate indicates the presence of zirconia nanoparticles [30]. For Mg doping, prepare three separate solutions of magnesium nitrate

hexahydrate in deionized water with doping concentrations (1 %, 3 %, and 5 %) and gradually add the magnesium nitrate solution to the Zirconium-*Eucalyptus* mixture under constant stirring. Later, the reaction mixture was allowed to sit undisturbed for 12 h to ensure complete precipitation and stabilization of nanoparticles. Centrifuge the reaction mixture (at 7000 rpm for 10 min) to separate the nanoparticles, followed by washing the nanoparticles multiple times with deionized water and ethanol to eliminate unreacted precursors and impurities. The nanoparticles are then dried at 80 °C. Further, the dried nanoparticles are calcined at 700 °C. This step crystallizes the nanoparticles, enhancing their stability and functional properties [31,32]. Here, ZrO_2 NPs are represented as Z, and different Mg concentrations (1 %, 3 %, and 5 %) are denoted as ZM1, ZM2, and ZM3, respectively.

2.4. Characterization techniques

Various advanced characterization techniques were employed to evaluate the properties of the nanocatalyst. X-ray diffraction using the X'Pert PRO (Netherlands) was employed to assess the crystal phase. Fourier Transform Infrared Spectroscopy (Spectrum 100, USA) was used to identify the vibrations of molecules and functional groups in the nanoparticles. Particle size analysis was conducted using Nanophox (Germany) to analyze the mean particle size, which analyzes the Brownian motion of nanoparticles in a colloidal suspension. The scattered light intensity provides information about particle size distribution. FESEM (Carl Zeiss, Sigma 300 (Germany)) to analyze the surface morphology of the nanoparticles. EDX integrated with FESEM to identify the elemental composition of the nanoparticles. UV–visible spectrophotometry (Cary 8454 (Agilent, Singapore)) was used to measure the optical absorbance of the synthesized nanoparticles. The spectrophotometer measures the absorbance of light across the UV–visible spectrum (200–800 nm).

2.5. Antibacterial activity

The antibacterial behavior of the synthesized Mg-doped ZrO_2 nanocomposites was assessed using the well-diffusion method. The bacterial strains were first cultured in Nutrient Broth to promote their growth, and then incubated at 36 °C for 12 h to ensure sufficient bacterial multiplication. Mueller-Hinton Agar (MHA), a nutrient-rich medium, was prepared and solidified in Petri dishes. The pre-cultivated bacterial strains were then evenly inoculated into the solidified MHA medium. Further, wells were carefully created on the inoculated agar plates, and the synthesized NPs were prepared at various concentrations (25, 50, and 100 mg/mL). A fixed volume of the NPs solution at each concentration was added to the respective wells. Streptomycin (S25 mcg), a standard antibacterial agent, was used to compare the effectiveness of the NPs. The nanoparticle-treated plates were incubated at 36 °C for 24 h, allowing the bacteria to grow and interact with the NPs. After incubation, the plates were examined for clear zones around the well. The zone of inhibition (ZOI) indicates the area where bacterial growth was inhibited by the NPs [33,34].

2.6. Photocatalytic activity

The catalytic behavior of the prepared nanoparticles was evaluated by assessing their ability to degrade two model dyes, Brilliant Blue (anionic) and Rhodamine B (cationic), under sunlight. Separate solutions of each dye were prepared in distilled water, maintaining a standard concentration of 20 mg/L (20 ppm). 100 mL of each dye solution was exposed to direct sunlight without adding any NPs to assess the natural degradation of the dyes under sunlight. Further, 100 mg of the synthesized NPs were added to 100 mL of each dye solution in separate beakers. These NPs-dye mixtures were then exposed to direct sunlight to activate the photocatalytic process. The mixtures were subjected to sunlight for 100 min, with samples collected every 10 min to monitor degradation progress. After each interval, the samples were analyzed using a UV–visible spectrophotometer to record changes in the dye's optical absorption spectrum [35]. The degradation efficiency (η) was calculated using the formula:

$$\eta = \frac{C_0 - C_t}{C_0} \text{ X } 100\%$$

Where, C_0 - Initial concentration of the dye. C_t - Dye concentration at a time.

2.7. Scavenging activity procedure

Active-species trapping experiments were carried out to identify the dominant ROS involved in the ZM3 photocatalytic process. In a typical run, 100 mg of the ZM3 catalyst was dispersed in 100 mL of a 20-ppm dye solution (BB and RhB) and ultrasonicated for 5 min. This was followed by stirring in the dark for 30 min to establish adsorption–desorption equilibrium. Specific scavengers were then introduced: isopropanol (IPA, 10 mM) as a hydroxyl radical (*OH) scavenger, *p*-benzoquinone (p-BQ, 1 mM) as a superoxide radical ($*O_2^-$) scavenger, methanol (10 mM) as an electron (e^-) scavenger, and potassium iodide (KI, 1 mM) as a hole (h^+) scavenger. The suspensions were subsequently exposed to natural sunlight with continuous stirring for 100 min, and aliquots were withdrawn at 10-min intervals, centrifuged, and analyzed using UV–Visible spectrophotometry at the respective λ_{max} of each dye. The degradation efficiencies obtained in the presence of each scavenger were compared with the no-scavenger control to determine the relative contribution of each reactive species to the photocatalytic mechanism [36].

3. Results and discussion

3.1. Crystal phase analysis

The XRD spectra of the synthesized Z and ZM1, ZM2, and ZM3 nanocomposites are shown in Fig. 2. The peaks observed correspond to specific crystallographic planes of ZrO_2. The intensity and sharpness of the peaks indicate that the materials are crystalline in nature. Prominent diffraction peaks are typically associated with the monoclinic phases of ZrO_2 with a space group of P 1 21/c1 (JCPDS No. 37–148). 2θ positions for ZrO_2 include **30.2**°, **35.2**°, **50.2**°, **60.0**°, **62.9**°, and **74.7**°, which correspond to specific Miller indices (101), (002), (112), (211), (202), and (220). The peak at 28.2° is characteristic of the (−111) plane of the monoclinic phase of ZrO_2 [25,33]. The diffraction peak at 42.8° (200) corresponds to the cubic MgO (PDF#45–0946), indicating partial formation of MgO at higher doping levels. With increasing Mg doping (ZM1

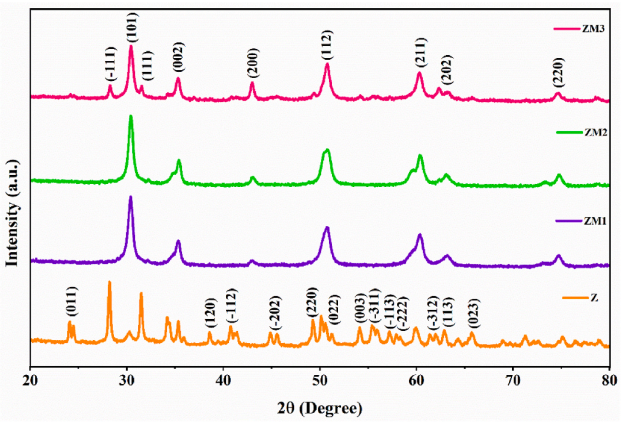


Fig. 1. XRD pattern of ZrO_2 and its nanocomposites.

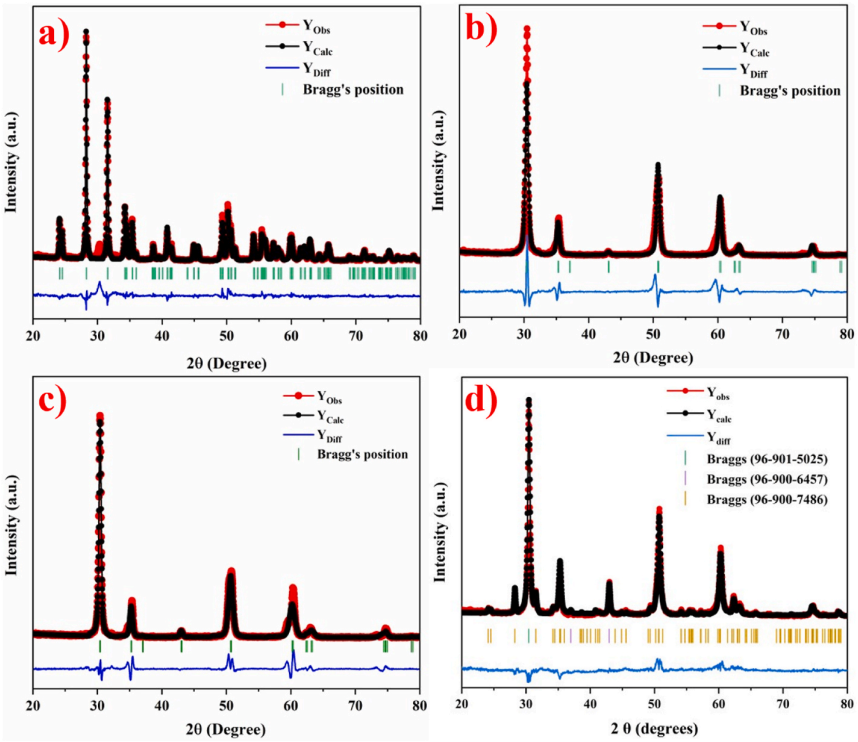


Fig. 2. Rietveld refinement of synthesized ZrO_2 (a), ZM1 (b), ZM2 (c), and ZM3 (d) nanocomposites.

→ ZM3), slight shifts in peak positions and variations in intensity are noticeable. The similar 2θ positions for all major peaks across the samples suggest that the low Mg doping levels and the slight ionic radius difference between Mg^{2+} (0.72 Å) and Zr^{4+} (0.84 Å) allow substitution without significant lattice distortion. Minor variations in peak intensity and broadening are observed with increased Mg content, which are attributed to lattice strain, oxygen-vacancy formation, and a reduction in crystallite size [37,38].

The average crystal size is calculated to be 32.27 nm (Z), 18.96 nm (ZM1), 14.53 nm (ZM2), and 11.8 nm (ZM3) using the Debye-Scherrer equation. When concentration increases, the crystal size decreases. At the highest Mg doping (ZM3), the crystal size further decreases because excessive Mg doping can lead to the formation of additional defects, including oxygen vacancies. From an application perspective, reduced crystallite size is favorable for both photocatalytic and antibacterial efficacy. In photocatalysis, the increased surface-to-volume ratio of smaller particles enhances the concentration of active sites for dye adsorption and the formation of ROS. The increased defect density in smaller crystallites facilitates charge separation and prolongs carrier lifetimes, hence allowing efficient production of *OH and $*O_2^-$ radicals. In terms of antibacterial activity, decreased particle size and increased defect density enhance proximity to bacterial cell membranes, concentrating reactive oxygen species at the bacteria catalyst interface and thereby enhancing oxidative damage. These factors help explain why ZM3, which has the smallest crystallite size and the highest defect density, exhibits the largest antibacterial zones of inhibition and superior photocatalytic efficiency, shown in Tables 2 and 3.

The prepared ZrO_2 and Mg–ZrO_2 (ZM1, ZM2, and ZM3) nanocomposites were used for qualitative analysis to perform Rietveld refinement on the XRD patterns, utilizing the Pseudo-Voigt function, as shown in Fig. 2. The space group of P 1 21/c 1 (14) with a monoclinic structure for pure ZrO_2 and a cubic structure with space group of Fm -3m (225) for the nanocomposite sample (ZM1, ZM2, ZM3). Table 1 depicts the refined parameters, which agree with prior findings.

Table 2
Nanocatalyst with kinetic rate constant and degradation efficiency for 100 min.

Sample	Dye used	Kinetic rate constant (x 10^{-2} min^{-1})	Degradation efficiency (%)	Stability efficiency after five cycles (%)
Z	BB	1.27	70.09	65.7
ZM 1		1.44	77.79	72.49
ZM 2		1.97	87.87	82.7
ZM 3		2.7	95.43	90.3
Z	RhB	1.57	78.97	73.45
ZM 1		1.8	84.45	79.9
ZM 2		2.13	89.96	84.66
ZM 3		3.01	97.08	92.18

Table 1
Refinement parameters of the synthesized nanoparticle and its nanocomposite.

Sample	Crystal size (nm)	Volume (10^6 p.m.^{3})	Dislocation density (x 10^{15} lines/m^2)	Lattice parameter (Å)	Rexp	Rp	Rwp	Chi^2
Z	32.27	140.7	0.96	a = 5.1480 b = 5.2100 c = 5.3160	8.12	6.92	9.86	1.21
ZM1	18.96	132.23	2.78	a = b = c = 5.0860	6.84	7.56	9.16	1.9
ZM2	14.53	132.37	4.74		8.12	6.83	9.78	1.2
ZM3	11.8	131.94	7.18		8.3	6.81	11.48	1.38

Table 3
A comparable assessment of the synthesized catalyst with previous literature outcomes.

Plant source	Nanoparticle	Nanoparticle Concentration	Dye	Dye concentration	Irradiation Light source	Irradiation time (min)	Degradation Efficiency (%)	Ref
Kappaphycus alvarezii	MgO	100 ppm	Rhodamine B	100 mg	Visible	180	94	[53]
			Methylene blue			150	98	
Ocimum basilicum seed	ZnO–MgO–Mn_2O_3	27.9 mg	Methylene blue	100 mL	UV	60	99	[54]
			Methyl orange			105	87.3	
			Rhodamine B			75	96.5	
			Eriochrome Black			90	97.2	
Morus nigra	CaO	0.4 g	Rhodamine B	100 mL	–	60	98.2	[55]
Cymbopogon citratus	ZnO/MgO (1:1 ratio)	0.6 g/L	Crystal violet	30-ppm	Sunlight	75	99.72	[26]
	ZnO/MgO (1:2 ratio)						97.04	
Gum *Moringa Oleifera*	TiO_2–ZrO_2	0.1 g	Methylene blue	20 mg/L	Sunlight	150	96.34	[56]
			Rhodamine B				94.52	
Ficus elastic	ZnO–ZrO_2	20 mg	Rhodamine 6G	50 mL	Solar	55	97.30	[57]
Diospyros kaki leaves	Zr–NiO/ZnO	20 mg	Brilliant green 4-nitrophenol	50 mL	Solar	90	86.4 89	[58]
Moringa oliefera	SnO_2	100 mg	Rhodamine B	60 mL	Solar	90	86	[59]
Ficus elastica	ZnO–ZrO2	20 mg	Rhodamine 6G	50 mL	Sunlight	330	98.94	[60]
Eucalyptus leaf	Z	100 mg	Brilliant Blue	100 mL	Visible	100	70.09	This work
	ZM1						77.79	
	ZM2						87.87	
	ZM3						95.43	
Eucalyptus leaf	Z	100 mg	Rhodamine B	100 mL	Visible	100	78.97	
	ZM1						84.45	
	ZM2						89.96	
	ZM3						97.08	

3.2. FTIR spectral analysis

The FTIR spectra of the prepared materials (Z, ZM1, ZM2, and ZM3) exhibit several characteristic peaks and are presented in Fig. 3. Notably, the intensity variations across the samples reflect differences in doping levels and structural modifications. The broad absorption band centered around 3405 cm^{-1} corresponds to the stretching vibrations of O–H groups. The wavenumber at 2926 cm^{-1} is defined as C–H stretching vibrations, likely due to organic residues. 1632 and 1382 cm^{-1} peaks represent the bending vibrations of adsorbed water molecules, further confirming the hydrophilic nature of the material surface. 1382 cm^{-1} peak is related to the symmetric stretching of carbonate groups (CO_3^{2-}).

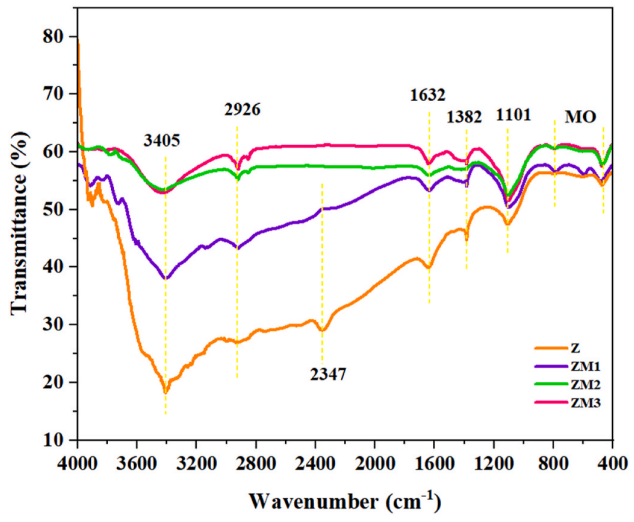


Fig. 3. FTIR spectrum of synthesized ZrO_2 and nanocomposite.

The sharp peak at 1101 cm^{-1} is characteristic of metal-oxygen (M − O) vibrations, indicating the Zr–O and Mg–O bonds, confirming the integration of Mg into the ZrO_2 lattice. Moreover, ZM3 shows more prominent peaks in the low-wavenumber region, suggesting enhanced metal-oxygen bonding due to higher Mg doping, which contributes to improved charge separation and photocatalytic activity [6,25,32].

3.3. FE-SEM analysis (Microstructure analysis)

The surface morphology was determined by FE-SEM analysis, and the micrographs are shown under similar magnification. Fig. 4a shows a relatively uniform distribution of quasi-spherical particles with a smooth surface. The smooth morphology is characteristic of undoped ZrO_2. Similar to ZrO_2 (Fig. 4b), quasi-spherical particles are retained, but the increased agglomeration compared to pure ZrO_2 suggests that Mg doping has introduced interparticle interactions. Fig. 4c) shows that the less spherical and rougher particles indicate that further Mg doping has disrupted the lattice structure, increasing surface defects [25,39]. Fig. 4d) shows the elongated particle morphology, which could be attributed to the highest level of Mg doping. This morphology suggests that doping has a strong influence on particle shape and structure at higher concentrations. Thus, increased doping levels result in stronger interparticle forces due to changes in surface charge, contributing to agglomeration [40].

From an application perspective, this morphological evolution is advantageous for both photocatalysis and antibacterial activity. Higher doping levels result in rough, defect-rich surfaces that offer increased active sites for dye adsorption, enhance light harvesting, and promote charge separation, which leads to improved ROS generation. The morphological features enhance contact with bacterial membranes, thereby supporting superior photocatalytic performance and antibacterial efficacy [39,40].

The EDS analysis confirms the elemental composition and weight percentage of the synthesized samples, as well as the successful

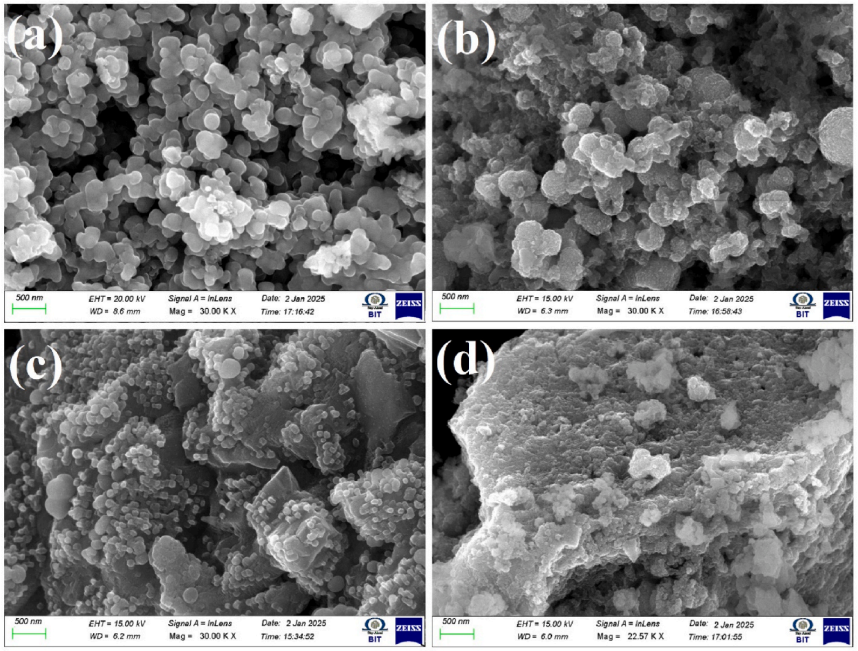


Fig. 4. Morphology analysis of synthesized ZrO_2 and nanocomposite.

incorporation of Mg into the ZrO_2 matrix at varying doping levels, which are analyzed and illustrated in Fig. 5. The spectrum for pure ZrO_2 (Fig. 5a) reveals only the presence of Zr (50.41 wt%) and oxygen (49.59 wt%). Where oxygen shows a higher content, confirming the formation of ZrO_2. For ZM1 (Fig. 5b), a small peak corresponding to Mg is observed, indicating low-level doping. The appearance of a small Mg peak (2.33 wt%) alongside O (52.11 wt%) and Zr (45.56 wt%) confirms the successful doping of Mg at a low concentration. In ZM2 (Fig. 5c), the Mg peak (4.09 wt%) becomes more pronounced, indicating a higher Mg concentration than in ZM1. This suggests successful doping with increased Mg incorporation. Finally, ZM3 (Fig. 5d) exhibits the highest Mg content (10.24 wt%), confirming a significant increase in Mg doping compared to the other samples. The EDS results conclusively demonstrate the successful doping of Mg into the ZrO_2 matrix [26].

Fig. 6 shows the elemental mapping of synthesized ZM3 nanocomposites. The combined elemental map (Fig. 6a) represents the distribution of Zr, O, and Mg within the sample. The overlay confirms that Zr and O form the primary ZrO_2 matrix, with Mg as an introduced dopant. The green colour (Fig. 6b) indicates the presence of oxygen (O) throughout the sample. The blue colour (Fig. 6c) represents Zr, which is evenly distributed throughout the sample. This indicates that the ZrO_2 matrix is homogeneously formed and serves as the dominant phase of the material. The red colour (Fig. 6d) represents Mg, which appears localized in specific regions rather than being uniformly distributed.

3.4. UV–visible spectral analysis

The UV–visible spectra of ZrO_2 and Mg–ZrO_2 (ZM1, ZM2, ZM3) samples reveal distinct absorbance peaks (Fig. 7), indicating changes in the electronic structure with increasing Mg doping. The ZrO_2 spectrum

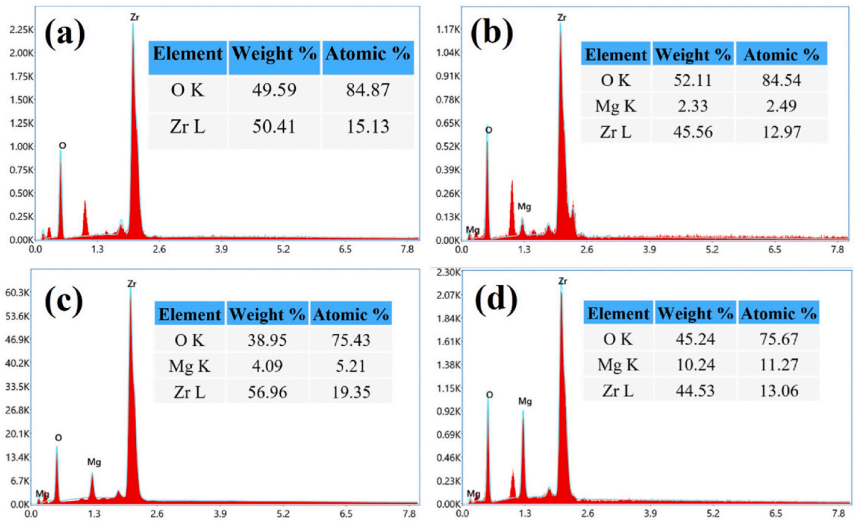


Fig. 5. EDS analysis for synthesized ZrO_2 and its nanocomposite.

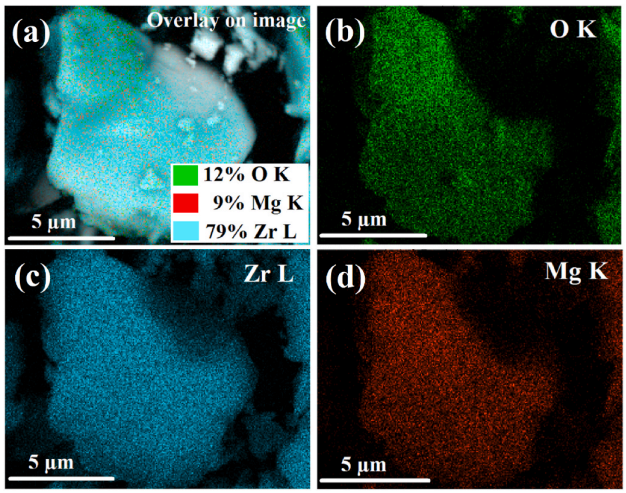


Fig. 6. Elemental mapping analysis of synthesized ZM3 nanocomposite.

shows a strong absorption peak at 201 and 273 nm. The peak at 201 nm is attributed to the charge transfer between Zr^{4+} and O_2^- in the ZrO_2 lattice, and the peak at 273 nm corresponds to defect states or oxygen vacancies present in ZrO_2, which can influence optical properties [29]. The ZM1 absorption peak is redshifted slightly to 226 nm compared to ZrO_2. This shift suggests slight variations in the electronic band structure resulting from the addition of Mg ions. The peak at 275 nm represents localized energy states introduced by Mg ions. The peak shifts to 362 nm, indicating a stronger interaction between Mg ions and the ZrO_2 matrix. The absorption peak shifts further to 368 nm, marking the most significant red shift among the samples. This shift is due to the increased substitution of Zr^{4+} by Mg^{2+} ions in the ZrO_2 lattice, which lowers the energy gap by creating defect levels near the conduction band. Mg doping introduces oxygen vacancies and other defects into the ZrO_2 matrix, creating localized energy states within the bandgap and reducing the effective optical bandgap [41,42].

3.5. DLS analysis

The average size (d_{50}) distribution of synthesized ZrO_2 and ZM nanocomposites is shown in Fig. 8. The particle size distribution analysis, represented by the d_{50} values, shows a progressive decrease in particle size with increasing Mg doping concentrations in ZrO_2. The d_{50} values reduce from 48.12 nm for pure ZrO_2 to 21.56 nm for the highest Mg-doped (Z3) sample. This reduction in particle size can be attributed to the influence of Mg ions, which disrupt the crystallization and grain growth of ZrO_2 due to their smaller ionic radius [17,33].

3.6. X-ray photoelectron spectroscopy (XPS) analysis

XPS analyses the top few nanometers of a surface, providing information on elemental composition and chemical states via binding energy (BE). The wide-scan (survey) spectrum (Fig. 9a) reveals O 1s, Mg 1s, and Zr 3d signals, therefore validating the expected elements of the heterostructure. The high-resolution O 1s spectrum (Fig. 9b) is separated into two primary components. The low-BE peak at 529.2 eV is associated with lattice O^{2-} in Mg–O and Zr–O environments. The peak at 531.3 eV is attributed to defect-related oxygen and surface OH/adsorbed species. These species are advantageous for catalytic processes; oxygen vacancies enhance charge separation and electron donation, while surface –OH groups serve as reaction/adsorption sites, accelerating the generation of reactive oxygen species. The Mg 1s core level (Fig. 9c) at 1303.9 eV is indicative of Mg^{2+} in MgO, indicating the presence of Mg as an oxide rather than in its metallic form or as suboxides.

The singular symmetric envelope and absence of a higher binding energy shoulder, often associated with $Mg(OH)_2/MgCO_3$, suggest a predominantly oxide environment with minimal secondary surface phases. A little BE shift in relation to bulk MgO may result from interfacial Mg–O–Zr bonding and localized lattice strain, indicating electronic interaction across the heterojunction [26]. The Zr 3d region (Fig. 9d) displays the predicted spin-orbit doublet, with Zr $3d_{5/2}$ at about 181.3 eV and Zr $3d_{3/2}$ at approximately 183.7 eV (splitting approximately 2.4 eV), aligning with Zr^{4+} in ZrO_2. Significantly, no further components at lower binding energy are detected, suggesting that decreased Zr^{3+} species are negligible and that stoichiometric ZrO_2

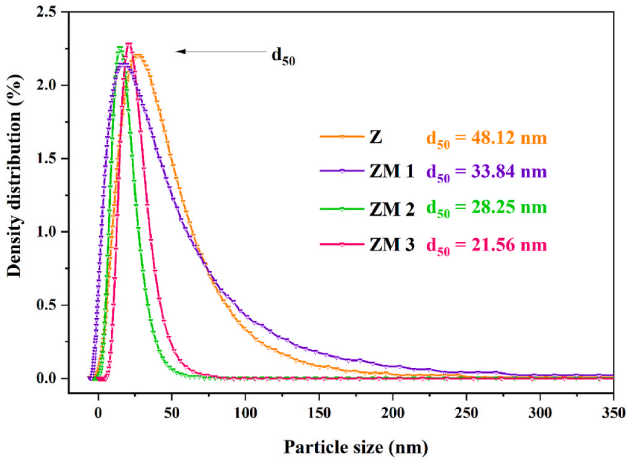


Fig. 8. Particle size distribution of synthesized ZrO_2 and its ZM nanocomposites.

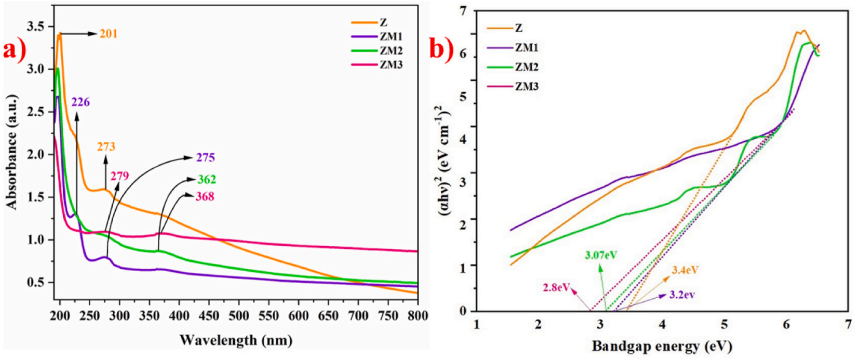


Fig. 7. Absorption spectrum of synthesized ZrO_2 and its nanocomposite.

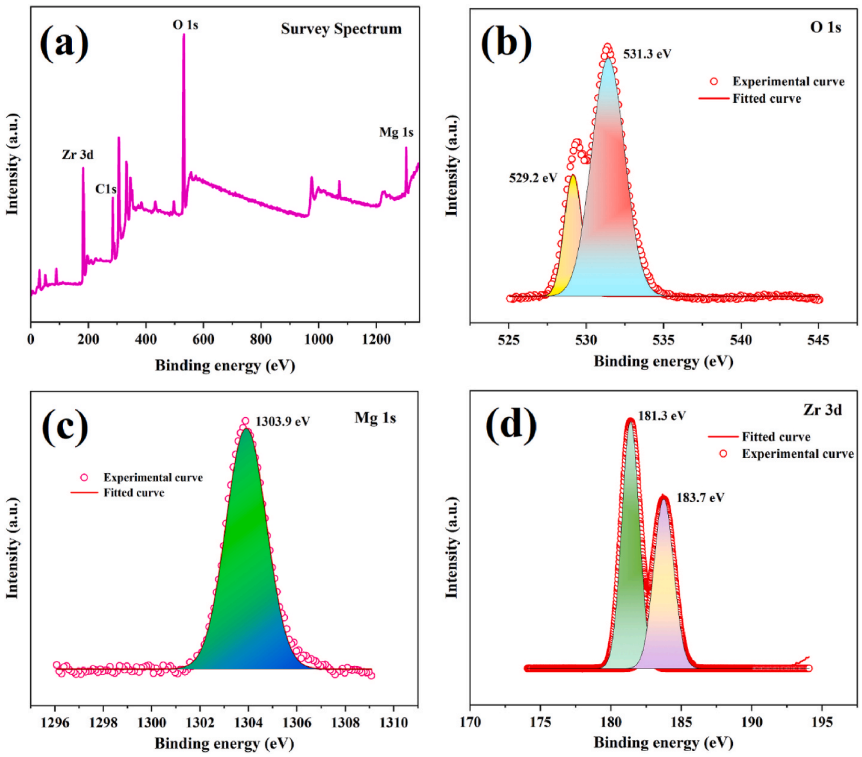


Fig. 9. XPS of the prepared ZM3 Nanocomposite.

primarily characterizes the surface. The survey and primary analyses validate a pristine ZM heterostructure characterized by Mg^{2+}/Zr^{4+} oxidation states, contributions from lattice oxygen and –OH, as well as significant interfacial electronic coupling [43,44]. Defect-rich, hydroxylated surfaces and Mg–O–Zr bonds are expected to enhance adsorption, accelerate interfacial charge transfer, and therefore boost photocatalytic efficacy.

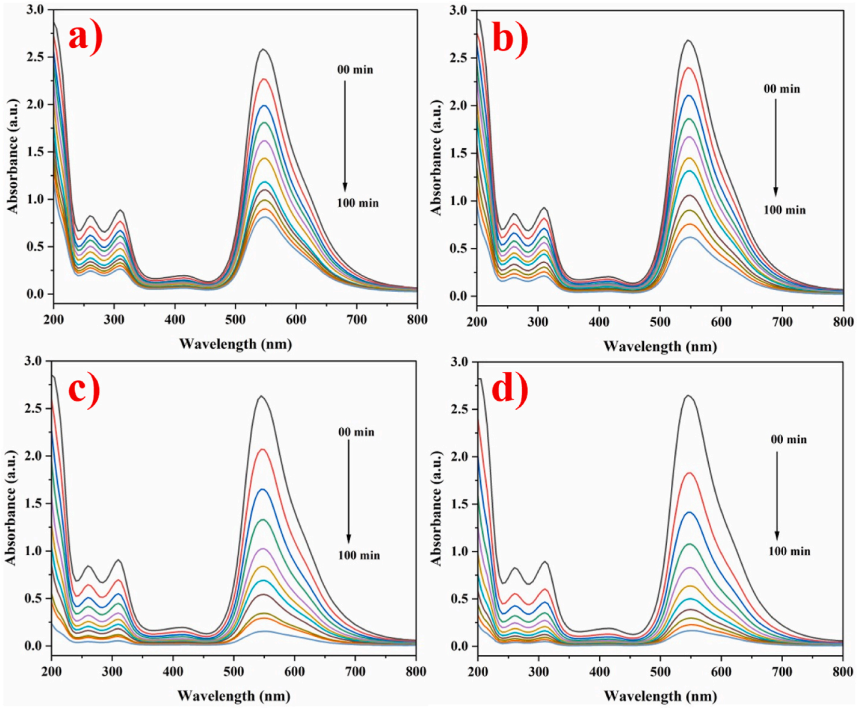


Fig. 10. Time-dependent degradation graph for BB dye. a) Z; b) ZM1; c) ZM2 and d) ZM3 nanocomposite.

3.7. Dye degradation activity

The catalytic efficiency of ZrO_2 and Mg–ZrO_2 (ZM1, ZM2, and ZM3) nanocomposites was evaluated using RhB and BB as model pollutants. The UV–visible absorbance spectra of the dye solutions treated with the nanocatalyst under direct sunlight irradiation (Figs. 10 and 11) showed a significant reduction in absorbance over a fixed time of 100 min, indicating effective dye degradation **with an interval of 10 min**. Fig. 12 (a & c) illustrates the C/C_0 graph, which progressively decreases with increasing irradiation time due to the absorption of photons, generating electron-hole pairs that facilitate the interruption of dye molecules.

Fig. 13 (a & b) presents the pseudo-first-order kinetic fitting data curves, showing a progressive increase with specific irradiation time, and the photocatalytic method follows pseudo-first-order kinetics.

$$\ln\left(\frac{C}{Co}\right) = -kt$$

The equation shows a log of dye concentration (C) to initial concentration (C_0) and the constant rate of reaction (k) with specific irradiation time (t). The results demonstrate a progressive improvement in photocatalytic activity with increasing Mg doping concentrations. For BB, ZrO_2 exhibits a kinetic rate constant of 1.27 x 10^{-2} min^{-1} and a degradation efficiency of 70.09 %, while the values progressively improve for ZM1 (1.44 x 10^{-2} min^{-1} with 77.79 % efficiency), ZM2 (1.97 x 10^{-2} min^{-1}; 87.87 %), and ZM3 (2.7 x 10^{-2} min^{-1}; 95.43 %). Similarly, for RhB, the kinetic rate constant increases from 1.57 for ZrO_2 to 1.8 for ZM1, 2.13 for ZM2, and 3.01 x 10^{-2} min^{-1} for ZM3 nanocomposite. The corresponding degradation efficiencies also increase from 78.97 % for Z to 84.45 %, 89.96 %, and 97.08 % for ZM1, ZM2, and ZM3, respectively. The kinetic data show that ZM3 achieves the highest degradation rate, as indicated by its highest rate constants (2.7 x 10^{-2} min^{-1} for BB dye and 3.01 x 10^{-2} min^{-1} for RhB). Table 2 presents the nanocatalyst data for the kinetic constant and degradation efficiency.

In undoped ZrO_2, these pairs tend to recombine quickly, limiting their effectiveness. Mg introduces defects into the ZrO_2 lattice, creating additional active sites and enhancing the separation of photogenerated electron-hole pairs. The increased number of active sites enhances the interface between the dye molecules and the photocatalyst, resulting in faster degradation. This reduces charge recombination and increases the production of ROS (superoxide anions ($*O_2^-$) and hydroxyl radicals (*OH)), which are responsible for breaking down dye molecules, and doping often results in structural changes, such as smaller particle sizes or increased porosity, which in turn increase the surface area of the photocatalyst. A larger surface area provides more adsorption sites for dye molecules, improving the catalyst's interaction with pollutants and enhancing the rate of degradation. Furthermore, cationic dyes (RhB) may have a higher susceptibility to attack by ROS due to their strong adsorption on the catalyst surface [45–47].

3.8. Scavenging activity and degradation mechanism

The degradation mechanism of the prepared photocatalyst with BB and RhB dyes is shown in Fig. 14. Upon illumination, photons with energy equal to or greater than the bandgap of the nanocatalyst are absorbed, exciting electrons (e^-) from the valence band (VB) to the conduction band (CB) and leaving behind positively charged holes (h^+) in the VB. This photoexcitation initiates the redox processes responsible for dye degradation. The photogenerated CB electrons migrate to the catalyst surface, where they reduce dissolved oxygen molecules to superoxide radicals ($*O_2^-$). Simultaneously, the VB holes oxidize surface hydroxyl groups (-OH) or water molecules to form highly reactive hydroxyl radicals (*OH). The doping further enhances the photocatalytic efficiency by introducing oxygen vacancies and structural defects into the material. These defects act as charge traps, which sustain the photogenerated electrons and significantly reduce the recombination rate of these electrons. The ROS species actively attack the aromatic rings and chromophoric structures of textile dye pollutants, breaking their complex molecular framework into smaller intermediate compounds. These intermediates undergo further oxidation by ROS, eventually yielding environmentally benign end products, including water and carbon dioxide [48–50].

Scavenging experiments were conducted to identify the primary

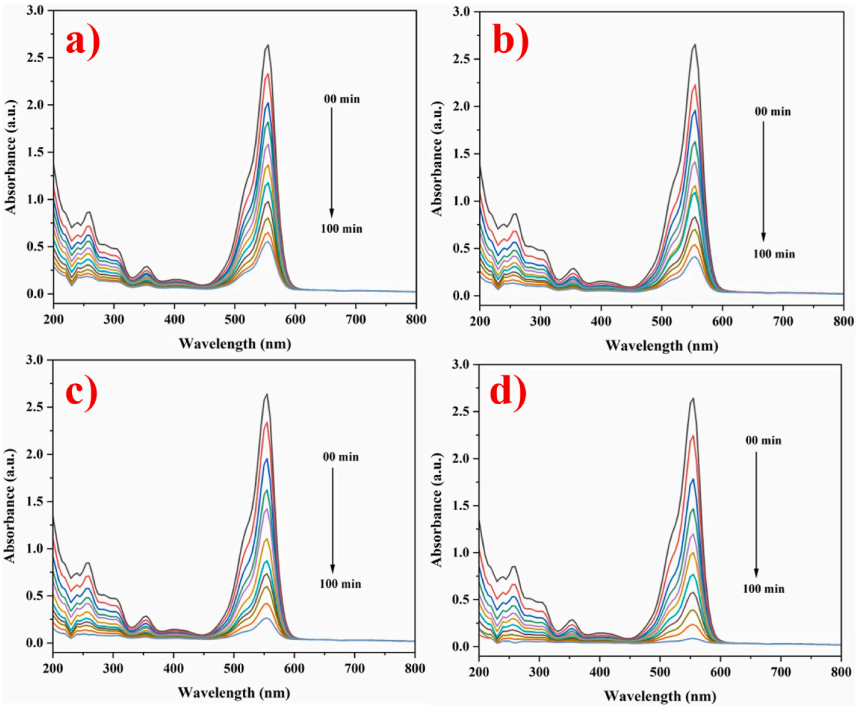


Fig. 11. Time-dependent degradation graph for RhB dye. a) ZrO_2; b) ZM1; c) ZM2 and d) ZM3 nanocomposites.

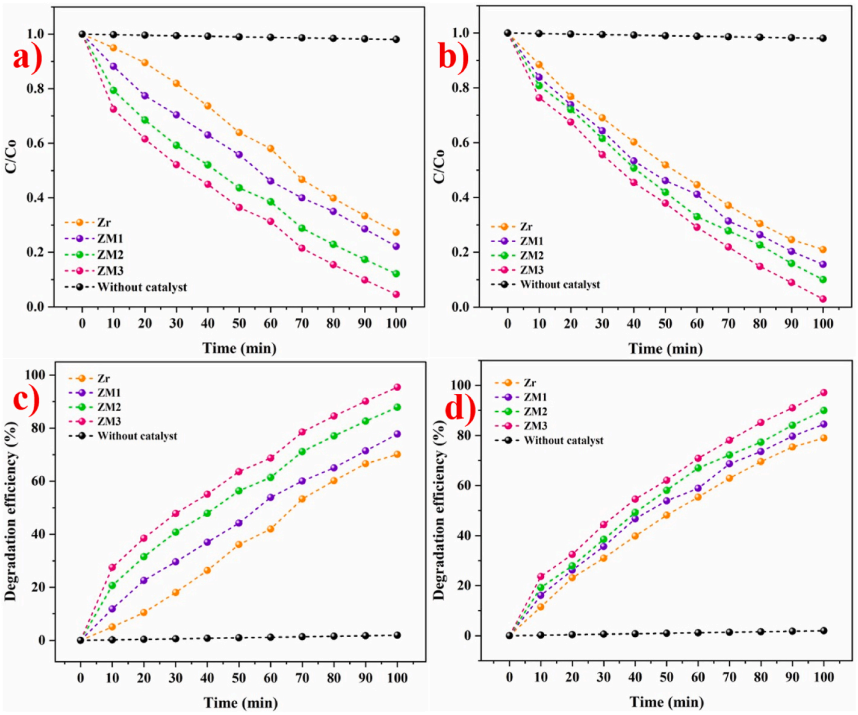


Fig. 12. C/C_0 and efficiency graph for BB (a & c) and RhB dye (b & d).

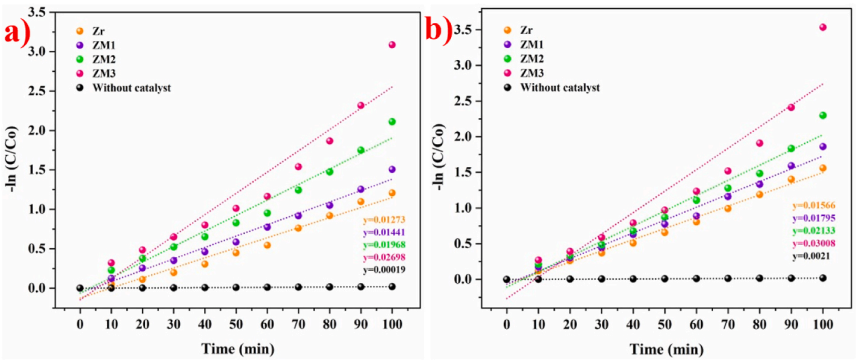


Fig. 13. Kinetics graph for BB (a) and RhB dye (b).

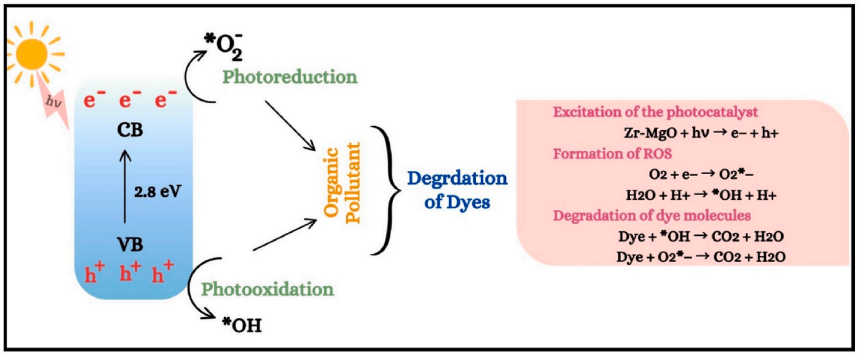


Fig. 14. Degradation mechanism of the prepared photocatalyst nanocomposite.

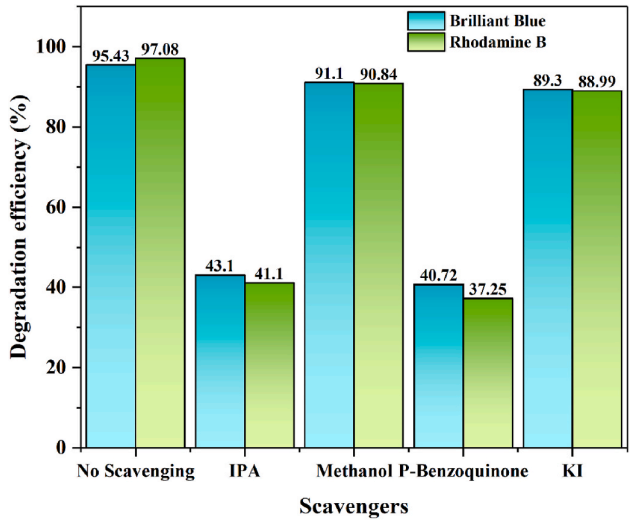


Fig. 15. Scavenging activity efficiency of ZM3 nanocomposite.

reactive species involved in ZM3 photocatalysis (Fig. 15). ZM3 demonstrated high degradation efficiencies of 95.43 % for BB and 97.08 % for RhB in the absence of scavengers, indicating its significant photocatalytic activity. The incorporation of IPA significantly decreased the efficiencies, suggesting that *OH is the primary oxidizing species. The addition of p-BQ resulted in a significant decrease, thereby confirming the predominant role of $*O_2^-$. Methanol moderately decreased the efficiencies, indicating that direct electron-mediated degradation is less critical than ROS-driven mechanisms. The addition of KI reduced the efficiencies, suggesting that surface-bound holes (h^+) contribute, yet to a lesser extent. The prevalence of *OH and $*O_2^-$ is due to their significant oxidative potential [47,51].

The dominance of *OH is due to its high oxidation potential (+2.8 V vs NHE), which enables the non-selective oxidation of dye molecules. $*O_2^-$ contributes to degradation both directly and indirectly by producing additional *OH through secondary reactions. The ZM3 photocatalytic mechanism is primarily influenced by *OH and $*O_2^-$ radicals, while electrons and h^+ serve secondary functions. The high efficiency of ROS generation is due to Mg-induced oxygen vacancies and defect states, which improve charge separation and prolong the stability of reactive species [52,53].

The photocatalytic degradation efficiency of the synthesized nanomaterials was validated by comparing the results obtained in this study with those previously reported in the literature. A comparative evaluation is crucial to demonstrate the relative performance and advancements achieved through the present green synthesis method, as shown in Table 3. This comparison examines key parameters, including catalyst type, target pollutant, irradiation conditions, and degradation percentage. The findings presented in Table 3 indicate that this study demonstrates enhanced photocatalytic activity compared to previous research, suggesting its potential application in wastewater treatment and environmental remediation.

3.9. Photocatalytic degradation stability and reusability

The cyclic stability of the synthesized photocatalysts was evaluated by assessing their photocatalytic degradation efficiency over five consecutive cycles using RhB and BB, as shown in Fig. 16. The results provide valuable insights into the durability and reusability of the materials under photocatalytic conditions. For RhB degradation, the percentage loss in photocatalytic efficiency after five cycles was observed to be 7.52 %, 6.01 %, 5.31 %, and 4.03 % for Z, ZM1, ZM2, and ZM3, respectively. Similarly, BB degradation occurred with efficiency losses of 8.22 %, 7.49 %, 6.45 %, and 5.16 % for the same samples. These findings indicate that cyclic stability improves significantly with increasing Mg doping, with ZM3 exhibiting the least loss of efficiency for both dyes.

The enhanced stability of the samples can be attributed to the

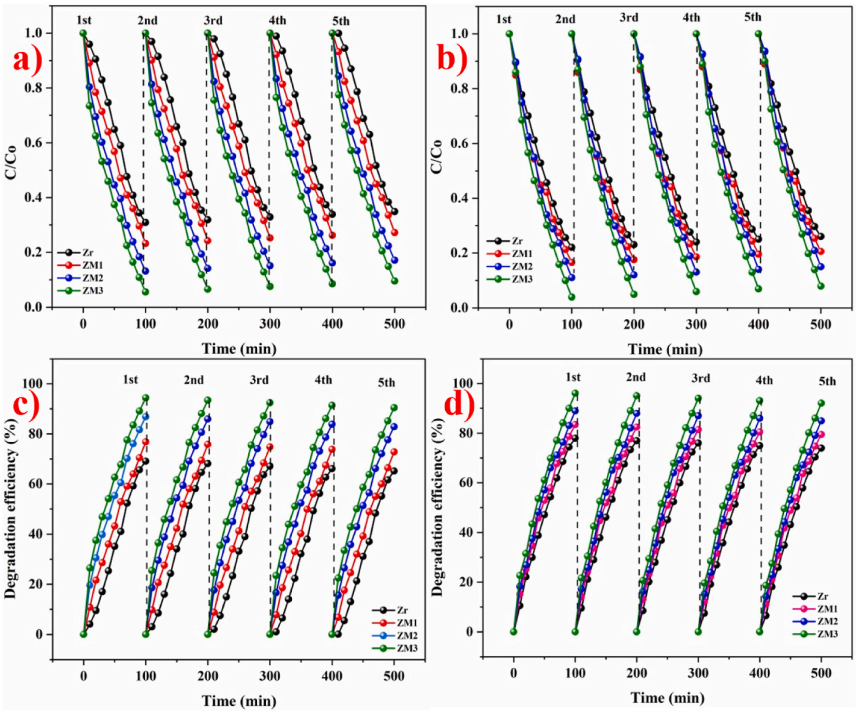


Fig. 16. Stability for nanocatalyst: C/C_0 and efficiency for BB (a & c) and RhB dye (b & d).

improved structural integrity and reduced susceptibility to photo-corrosion resulting from the incorporation of Mg. Mg doping introduces oxygen vacancies and structural defects that enhance the durability of the ZrO_2 matrix by providing additional charge-trapping sites and increasing resistance to photo corrosion [45]. These vacancies also improve the separation of photogenerated charge carriers, thereby reducing electron-hole recombination and preserving photocatalytic activity over prolonged use. The slight decrease in efficiency after repeated cycles is primarily due to the adsorption of degradation byproducts on the catalyst surface, which can block active sites and reduce light absorption. However, washing the samples with ethanol before each reuse effectively minimized these effects, maintaining consistent photocatalytic performance across multiple cycles.

In contrast, the undoped ZrO_2 exhibited the highest degradation loss due to its limited resistance to photo-corrosion and higher electron-hole recombination rates, thereby reducing its durability. Thus, Mg doping enhances the robustness and reusability, making ZM3 the most stable and efficient material for dye degradation under repeated use. The recycled samples underwent FTIR analysis, and the functional groups were investigated. Fig. 17 (a & b) presents the FTIR analysis of nanoparticles following photocatalysis, including BB and RhB dye.

By confirming the presence of functional groups and surface-bonded species in the as-prepared nanocomposites, which are directly related to their photocatalytic and antibacterial applications, FTIR analysis plays a significant role in this study. Lattice oxygen vibrations and surface hydroxyl groups (-OH) are necessary because they may serve as active sites for the production of *OH during photocatalysis. These groups facilitate the adsorption of water and dye molecules, which is essential for the efficient production of ROS when exposed to sunlight. Fig. 17 (c & d) presents the XRD analysis of nanoparticles following photocatalysis, including BB and RhB dyes. For both dyes, all Z and ZM patterns preserve the same 2θ positions as those in the previous spectra (Fig. 1). No new crystalline phases ($Mg(OH)_2$, $MgCO_3$, $Zr(OH)_4$) or dye-derived crystalline residues appear. This demonstrates that the ZM nanocomposite is crystallographically stable under the reaction conditions. The small peaks present are primarily related to surface-adsorbed dye residues after photocatalysis. Since the prominent ZrO_2/MgO peaks remain intact. XRD comparison demonstrates that Z, ZM1, ZM2, and ZM3 maintain their crystalline phases and heterostructure integrity after photocatalytic degradation of both BB and RhB dyes, with only minor surface related broadening, suggesting excellent structural stability and reusability of the catalysts.

Following photocatalytic activity, the FTIR spectrum of the used catalyst exhibits intensity fluctuations and, occasionally, minor peak shifts. Because they contribute to the production of ROS, these alterations may be linked to the partial removal or alteration of surface hydroxyl groups as well as the adsorption of dye degradation intermediates. While new or modified peaks in the fingerprint area can represent leftover organic molecules that were partially adsorbed on the catalyst surface, a reduction in the intensity of the –OH peak indicates that surface hydroxyls were consumed during the oxidation process [52].

3.10. Antibacterial behaviour

The antibacterial activity of the synthesized ZrO_2 and Mg–ZrO_2 (ZM1, ZM2, and ZM3) nanocomposites was evaluated against *Staphylococcus aureus* and *Escherichia coli* using the well-diffusion method. The graphical representation of the antibacterial activity is shown in Fig. 18. The ZOI of the samples is presented in Fig. 19. The standard streptomycin (S25) antimicrobial agent was used as a reference to compare the efficacy of the samples. The synthesized materials exhibit promising antibacterial activity, with enhanced performance against *Staphylococcus aureus* compared to *Escherichia coli*. The ZOI values increase with nanoparticle concentration, indicating concentration-dependent activity. For *Staphylococcus aureus*, the ZOI values for Z, ZM1, ZM2 and ZM3 were 12.4, 15.1, 16.8, and 19.2 mm at 100 μg/mL, respectively, compared to the standard S25 (11.3 mm), similarly, for *Escherichia coli*, the ZOI values measuring 11, 12.7, 14.6, and 18.3 mm for Z, ZM1, ZM2 and ZM3 respectively, at 100 μg/mL.

The increased antibacterial activity of the nanocatalyst is attributed to its enhanced generation of ROS under sunlight. Mg doping facilitates

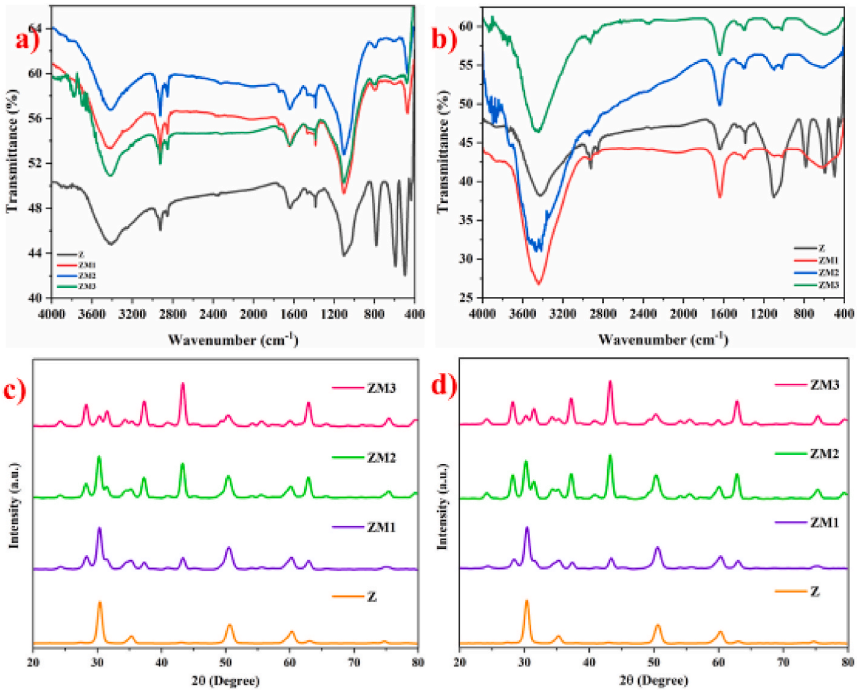


Fig. 17. XRD and FTIR analysis after photocatalytic activity for BB (a & c) and RhB (b & d).

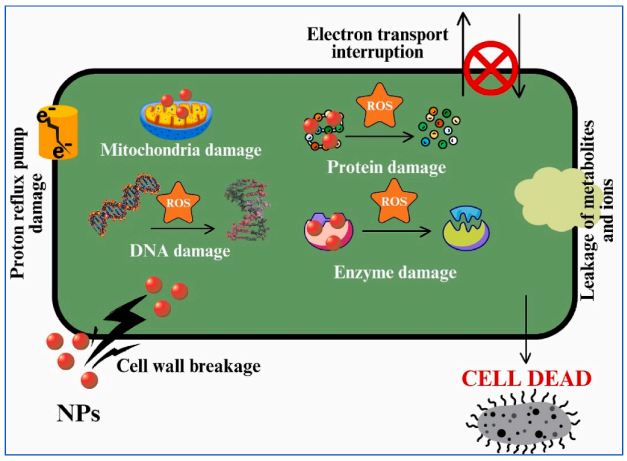


Fig. 18. Graphical representation of the antibacterial mechanism.

charge separation and reduces electron-hole recombination, thereby increasing ROS yield. These ROS attack bacterial membranes, causing lipid peroxidation and disrupting the structural integrity; this effect is more pronounced in Staphylococcus aureus due to its simpler membrane architecture. Once the membrane is compromised, ROS penetrate the cells and oxidize intracellular components, including proteins and DNA, ultimately leading to cell death [61,62]. Additionally, positively charged Mg^{2+} ions interact electrostatically with the negatively charged bacterial membrane, further enhancing membrane disruption and ROS penetration. Higher Mg doping in ZM3 amplifies these effects, making ROS production and membrane targeting critical factors in its superior antibacterial action. Fig. 20 presents the antibacterial plate images with the ZOI obtained.

Although *Staphylococcus aureus* and *Escherichia coli* are widely studied, they remain relevant due to their unique cell wall structures and resistance mechanisms. *Staphylococcus aureus*, a Gram-positive bacterium, possesses a thick peptidoglycan layer and no outer membrane, making it more susceptible to oxidative stress. At the same time, *Escherichia coli* has a thinner peptidoglycan layer but an outer membrane enriched with lipopolysaccharides that can hinder ROS penetration [63,64]. The higher doping level enhances the generation of ROS, resulting in greater damage to bacterial cells. Fig. 18 presents a graphic picture of the antibacterial mechanism.

4. Conclusion

Mg-doped ZrO_2 nanocomposites were synthesized using Eucalyptus

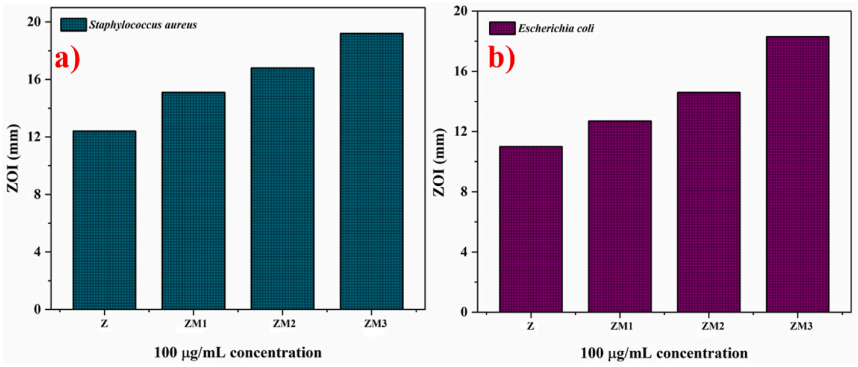


Fig. 19. Antibacterial ZOI activity of prepared samples against a) *Escherichia coli* and b) *Staphylococcus aureus*.

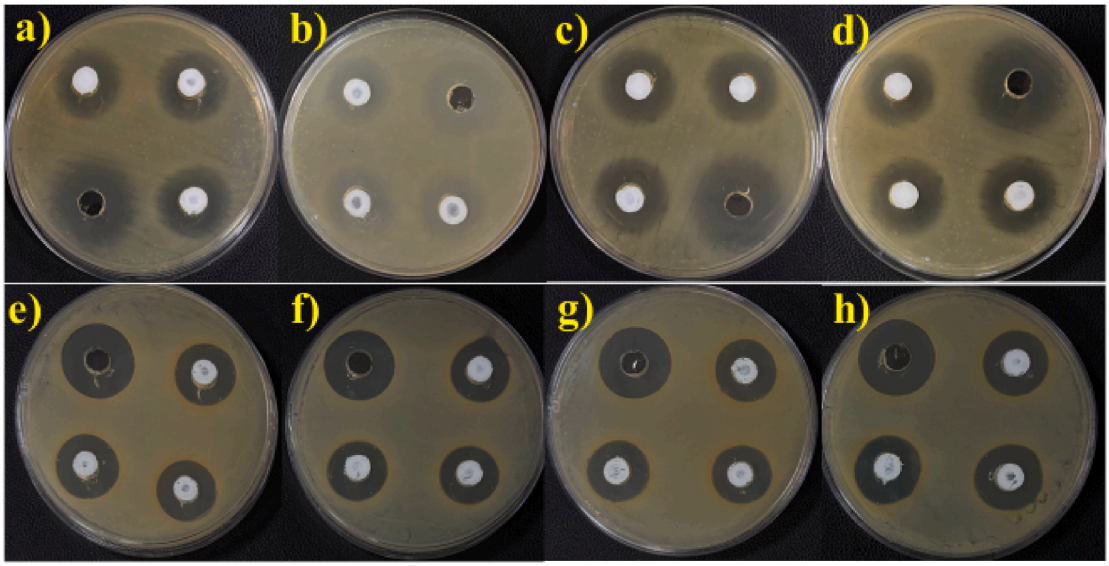


Fig. 20. Antibacterial images of Z, ZM1, ZM2, and ZM3 nanocomposites against *Staphylococcus aureus* (a–d) and *Escherichia coli* (e–h).

leaf extract, with a comprehensive characterization of their structural, optical, and functional properties. The presence of crystalline monoclinic and cubic phases is confirmed through XRD and Rietveld refinement analysis. XRD analysis confirmed the successful incorporation of Mg into the ZrO_2 lattice, evidenced by minor shifts in peak positions that suggest lattice distortion and the formation of oxygen vacancies. The average crystal size exhibited a progressive reduction with increasing Mg doping, decreasing from 32.27 nm for ZrO_2 to 11.8 nm for ZM3 due to lattice strain. FTIR analysis revealed the presence of Zr–O and Mg–O bonds, along with an increase in hydroxyl group intensity following repeated use, indicating surface modifications that improve photocatalytic performance. The UV–visible spectra indicate that Mg doping successfully modifies the optical properties of ZrO_2, demonstrating a notable narrowing of the bandgap with increased Mg concentration, as shown by the red shift in absorption peaks for ZM3 (368 nm), which enhances light absorption in the visible spectrum. FESEM analysis revealed a morphological transition from quasi-spherical particles in ZrO_2 to elongated structures in ZM3, with increased surface roughness and agglomeration, which enhances the availability of active sites for photocatalytic and antibacterial activity. The d_{50} values reduced from 48.12 nm for ZrO_2 to 21.56 nm for ZM3 following Mg doping. The reduction in size results from the substitution of Mg^{2+}, which inhibits grain growth and increases surface area and defect density, thereby improving functional performance. The photocatalytic performance of the samples, evaluated with BB and RhB dyes under sunlight, demonstrated maximum degradation efficiencies of 95.43 % and 97.08 % for ZM3, respectively, attributed to improved charge separation and reactive oxygen species generation. The cyclic stability tests demonstrated that ZM3 maintained over 90 % efficiency after five consecutive cycles, signifying superior reusability and structural integrity. Antibacterial studies indicated that ZM3 displayed the highest activity, with a ZOI of 19.2 mm for *Staphylococcus aureus* and 18.3 mm for *Escherichia coli*, demonstrating greater efficacy against Gram-positive bacteria attributed to their simpler membrane structure. These results demonstrate the potential of Mg–ZrO_2 nanocomposites as sustainable and multifunctional materials for environmental applications, such as wastewater treatment and antimicrobial resistance.

CRediT authorship contribution statement

M. Pushpa: Writing – original draft, Funding acquisition, Data curation, Conceptualization. **S. Mageswari:** Supervision, Project administration, Data curation, Conceptualization. **S. Na Shereenaa:** Writing – review & editing, Resources, Formal analysis. **S. Surendhiran:** Writing – review & editing, Methodology, Investigation.

Consent to publish

Not applicable.

Ethics approval and consent to participate

Not applicable.

Availability of data and materials

The datasets used or analyzed during the current study are available from the corresponding author upon reasonable request.

Funding information

This research did not receive any specific grant from funding agencies.

Conflict of interest

The authors declare that they have no known competing financial interests or personal relationships that could have appeared to influence the work reported in this paper.

References

[1] R.P. Schwarzenbach, T. Egli, T.B. Hofstetter, U. Von Gunten, B. Wehrli, Global water pollution and human health, Annu. Rev. Environ. Resour. 35 (1) (2010) 109–136.
[2] N. Kandhasamy, S. Srinivasan, G. Murugadoss, R. Venkatachalam, A non-aqueous nickel–manganese sulfide on rGO wrapped Ni-foam as a supercapacitor advanced electrode material, J. Mater. Sci. Mater. Electron. 33 (2022) 22941–22956, https://doi.org/10.1007/s10854-022-09064-1.
[3] S. Ying, Z. Guan, P.C. Ofoegbu, P. Clubb, C. Rico, F. He, J. Hong, Green synthesis of nanoparticles: current developments and limitations, Environ. Technol. Innovat. 26 (2022) 102336.
[4] K. Subramani, N.V. Tamilselvi Mohanasundaram, S. Srinivasan, J. Krishnaveni Selva Ganeshan, A. Incharoensakdi, Microalgae-based bio-fabrication using zinc oxide-chitosan nanocomposite for industrial effluent degradation and pollutant reduction, Int. J. Biol. Macromol. 319 (2025) 145379, https://doi.org/10.1016/j.ijbiomac.2025.145379.
[5] A.K. Chitoria, A. Mir, M.A. Shah, A review of ZrO2 nanoparticles applications and recent advancements, Ceram. Int. 49 (2023) 32343–32358, https://doi.org/10.1016/j.ceramint.2023.06.296.
[6] N. Tabassum, D. Kumar, D. Verma, R.A. Bohara, M.P. Singh, Zirconium oxide (ZrO2) nanoparticles from antibacterial activity to cytotoxicity: a next-generation of multifunctional nanoparticles, Mater. Today Commun. 26 (2021) 102156.
[7] M. Sajid, J. Płotka-Wasylka, Nanoparticles: synthesis, characteristics, and applications in analytical and other sciences, Microchem. J. 154 (2020) 104623.
[8] S. Jadoun, R. Arif, N.K. Jangid, R.K. Meena, Green synthesis of nanoparticles using plant extracts: a review, Environ. Chem. Lett. 19 (1) (2021) 355–374.
[9] V. Kavitha, J. Mayandi, P. Mahalingam, N. Sethupathi, Structural, optical, and electrical studies on zinc-doped barium strontium titanate as photo-anode for DSSC device, Mater. Today 35 (2021) 48–52.
[10] A.M.E. Shafey, Green synthesis of metal and metal oxide nanoparticles from plant leaf extracts and their applications: a review, Green Process. Synth. 9 (1) (2020) 304–339.
[11] J.O. Adeyemi, A.O. Oriola, D.C. Onwudiwe, A.O. Oyedeji, Plant extracts mediated metal-based nanoparticles: synthesis and biological applications, Biomolecules 12 (5) (2022) 627.
[12] H. Sawalha, R. Abiri, R. Sanusi, N.A. Shaharuddin, A.A.M. Noor, N.A. Ab Shukor, H. Abdul-Hamid, S.A. Ahmad, Toward a better understanding of metal nanoparticles, a novel strategy from eucalyptus plants, Plants 10 (5) (2021) 929.
[13] H.M. Abuzeid, C.M. Julien, L. Zhu, A.M. Hashem, Green synthesis of nanoparticles and their energy storage, environmental, and biomedical applications, Crystals 13 (11) (2023) 1576.
[14] Y. Zhang, J. Li, K. Lin, Magnesium-alloying induced photoelectronic modulation in sol-gel-processed ZnO: strain-mediated defect passivation and bandgap tailoring, J. Appl. Phys. (2025). https://pubs.aip.org/aip/jap/article/138/6/065101/3358327.
[15] D.H.K. Reddy, S.-M. Lee, Application of magnetic chitosan composites for the removal of toxic metal and dyes from aqueous solutions, Adv. Colloid Interface Sci. 201–202 (2013) 68–93, https://doi.org/10.1016/j.cis.2013.10.002.
[16] A.A. Barzinjy, H.H. Azeez, Green synthesis and characterization of zinc oxide nanoparticles using *Eucalyptus* globulus Labill. leaf extract and zinc nitrate hexahydrate salt, SN Appl. Sci. 2 (5) (2020) 991.
[17] R. Sagheer, M. Khalil, V. Abbas, Z.N. Kayani, U. Tariq, F. Ashraf, Effect of Mg doping on structural, morphological, optical and thermal properties of ZnO nanoparticles, Optik 200 (2020) 163428.
[18] M. Vinoth, S. Surendhiran, P.R. Senthilmurugan, V. Rajendran, Enhanced photovoltaic performance of hybrid solar cells with a calcium interfacial metal electrode, J. Electron. Mater. 48 (2019) 4589–4597.
[19] P. Bhowmik, B. Modi, P. Roy, A. Chowdhury, Strategies to combat Gram-negative bacterial resistance to conventional antibacterial drugs: a review, Osong Public Health Res. Perspect. 14 (2023) 333–346, https://doi.org/10.24171/j.phrp.2022.0323.
[20] M. Gopikrishnan, S. Haryini, G.P.D. C, Emerging strategies and therapeutic innovations for combating drug resistance in Staphylococcus aureus strains: a comprehensive review, J. Basic Microbiol. 64 (2024) e2300579, https://doi.org/10.1002/jobm.202300579.
[21] R.N. Abdrashitova, G.S. Bozhenkova, A.A. Ponomarev, A.G. Gilya-Zetinov, A. A. Markov, M.D. Zavatsky, Synthesis of ZNO doped multi walled carbon nanotubes (MWNTS) for dyes degradation and water purification, Water Conserv. Manag 7 (2023) 1–5. https://www.watconman.org/archives-pdf/1wcm2023/1wcm2023-01-05.pdf.
[22] H. Du, A. Zhang, Q. Zhang, Y. Sun, H. Zhu, H. Wang, Z. Tan, X. Zhang, G. Chen, Fabrication of recoverable Bi2O2S/Bi5O7I/ZA hydrogel beads for enhanced photocatalytic Hg0 removal in the presence of H2O2, Sep. Purif. Technol. 359 (2025) 130597, https://doi.org/10.1016/j.seppur.2024.130597.
[23] Z. Shan, Y. Yang, H. Shi, J. Zhu, X. Tan, Y. Luan, Z. Jiang, P. Wang, J. Qin, Hollow dodecahedra graphene oxide- cuprous oxide nanocomposites with effective

photocatalytic and bactericidal activity, Front. Chem. 9 (2021) 755836, https://doi.org/10.3389/fchem.2021.755836.
[24] M. Muthulakshmi, A.P. Sudha, S. Surendhiran, Synthesis and characterisation of ZnS nanoparticles: a comprehensive study on phase transition and photocatalytic degradation kinetics, J. Mater. Sci. Mater. Electron. 36 (2025) 1–25, https://doi.org/10.1007/s10854-025-15822-8.
[25] P. Chelliah, S.M. Wabaidur, H.P. Sharma, H.S. Majdi, D.A. Smait, M.A. Najm, A. Iqbal, W.C. Lai, Photocatalytic organic contaminant degradation of green synthesized ZrO_2 NPs and their antibacterial activities, Separations 10 (3) (2023) 156.
[26] T.V. Nitha, S. Britto, Enhanced photocatalytic degradation and biological activities of green synthesized mesoporous ZnO/MgO nanocomposites, J. Iran. Chem. Soc. 22 (4) (2025) 915–929.
[27] A. Muhaymin, H.E.A. Mohamed, K. Hkiri, A. Safdar, S. Azizi, M. Maaza, Green synthesis of magnesium oxide nanoparticles using *Hyphaene thebaica* extract and their photocatalytic activities, Sci. Rep. 14 (1) (2024) 20135.
[28] K. Kandasamy, S. Surendhiran, K.S.G. Jagan, G.S. Kumar, Y.A.S. Khadar, P. Rajasingh, Green synthesis of CdS quantum dots for photocatalytic and anti-corrosive applications in aqueous media, Appl. Surf. Sci. Adv. 13 (2023) 100364.
[29] A. Balamurugan, K.C. Suresh, K.S.G. Jagan, G.S. Sivagurunathan, R. Marnadu, T. M. Naren Vidaarth, S. Surendhiran, Y.A.S. Khadar, Detoxification of textile industry effluents using SnO2/carbon dots nanocomposites synthesized by green fabrication using Moringa leaves extract, J. Mater. Sci. Mater. Electron. 36 (2025), https://doi.org/10.1007/s10854-025-15171-6.
[30] S. Karthikeyan, K. Dhanakodi, S. Surendhiran, K.S.G. Jagan, N. Lenin, L. Dhatchinamurthy, A.T. Rajamanickam, Sonochemical synthesis of Sn-doped La2O3 nanoparticles and its application for the photocatalytic degradation of hazardous pollutants, J. Mater. Sci. Mater. Electron. 34 (2023), https://doi.org/10.1007/s10854-023-10561-0.
[31] K. Subramani, R. Saha, S. Palanisamy, B. Kolathupalayam Shanmugam, S. Rangaraj, V. Murugan, S. Srinivasan, R. Venkatachalam, W.K. Aicher, Wet chemical preparation of herbal nanocomposites from medicinal plant leaves for enhanced coating on textile fabrics with multifunctional properties, SN Appl. Sci. 2 (2020), https://doi.org/10.1007/s42452-020-2459-z.
[32] A.K. Chauhan, N. Kataria, V.K. Garg, Green fabrication of ZnO nanoparticles using *Eucalyptus* spp. leaves extract and their application in wastewater remediation, Chemosphere 247 (2020) 125803.
[33] N. Hossain, M.A. Chowdhury, A. Hossain, M.H. Mobarak, M.A. Islam, M. Abdullah, M.M. Rahman, Green synthesis and characterization of Alocasia indica assisted zirconium dioxide nanoparticles for improved antimicrobial application, Nano LIFE 14 (3) (2024) 2450006.
[34] Chavanich Kalidasan, K.S.G. Jagan, Surendhiran, T.M. Naren Vidaarth, Kathiresan Karthik, J.W.H. Yong, Viyakarn, Evaluation of biogenic zinc oxide nanoparticles from Sonneratia ovata leaf extract for multivariate factorial photocatalytic and biological activities, Biocatal. Agric. Biotechnol. 69 (2025) 103759, https://doi.org/10.1016/j.bcab.2025.103759.
[35] Y. Sun, H. Zheng, Y. Pu, H. Yang, J. Wang, S. Zhou, Q. Li, C. Qiao, Ultrahigh adsorption capacity zirconium-magnesium composite oxide nanoclusters remove malachite green from aqueous media, Adsorpt. Sci. Technol. (2022) 1946955, 2022.
[36] Y. Ren, Y. Chen, Q. Li, H. Li, Z. Bian, Microwave-assisted photocatalytic degradation of organic pollutants via CNTs/TiO2, Catalysts 12 (2022) 940, https://doi.org/10.3390/catal12090940.
[37] A. Venkatesan, N.R. Krishna Chandar, A. Jagadesan, K. Pradeeswari, P. Pandi, R. Manmohan, A. Kandasamy, R. Mohan Kumar, R. Jayavel, Self-assembled hierarchical microporous ZrO_2 nanoparticles and Mg-doped ZrO2 nanodiscs synthesized by non-aqueous sol–gel route, J. Mater. Sci. Mater. Electron. 33 (17) (2022) 14295–14304.
[38] L. Keerthana, C. Sakthivel, I. Prabha, MgO-ZrO2 mixed nanocomposites: fabrication methods and applications, Mater. Today Sustain. 3 (2019) 100007.
[39] G. Vignesh, G. Rajesh, M.K. Kumar, Mn, Mg-doped ZrO 2 nanoparticles: a photostable catalyst for enhanced mineralization and photocatalytic degradation of MV and MB dyes under sunlight irradiation, J. Mater. Sci. Mater. Electron. 32 (2021) 27044–27059.
[40] M.S. Mostari, M.J. Haque, S.R. Ankur, M.A. Matin, A. Habib, Effect of mono-dopants (Mg2+) and co-dopants (Mg2+, Zr4+) on the dielectric, ferroelectric and optical properties of BaTiO3 ceramics, Mater. Res. Express 7 (6) (2020) 66302S.
[41] G. Rajesh, S. Akilandeswari, D. Govindarajan, K. Thirumalai, Enhancement of photocatalytic activity of ZrO2 nanoparticles by doping with Mg for UV light photocatalytic degradation of methyl violet and methyl blue dyes, J. Mater. Sci. Mater. Electron. 31 (2020) 4058–4072.
[42] Z. Song, S. Liu, B. Huang, J. Wang, B. Han, G. Yan, Y. Sun, Optimized preparation of MgO-ZrO2 nanocomposite powders by assisted sol-gel method, J. Phys. Conf. 2390 (1) (2022, December) 012050. IOP Publishing.
[43] H.S. Lokesha, K.R. Nagabhushana, F. Singh, S.H. Tatumi, A.R.E. Prinsloo, C. J. Sheppard, Unraveling the charge state of oxygen vacancies in monoclinic ZrO_2 and spectroscopic properties of ZrO_2:Sm^{3+} phosphor, J. Phys. Chem. C Nanomater. Interfaces 125 (2021) 27106–27117, https://doi.org/10.1021/acs.jpcc.1c07365.
[44] T. Huma, N. Hakimi, M.A. ul Haq, T. Huma, L. Xu, X. Zhu, Synthesis and characterization of MgO-ZrO2 heterostructure: optical, mechanical and electrical properties, Crystals (2025), https://doi.org/10.3390/cryst15050465.
[45] V. Gowthambabu Surendhiran, A. Balamurugan, M. Sudha, V.B. Senthil Kumar, K. C. Suresh, Rapid green synthesis of CuO nanoparticles and evaluation of its photocatalytic and electrochemical corrosion inhibition performance, mater, Today Off. 47 (2021) 1011–1016.
[46] S. Karthikeyan, K. Dhanakodi, S. Surendhiran, K.S.G. Jagan, P. Thirunavukkarasu, L. Arunraja, Effect of synthesis parameters on the structural, morphological characteristics, and photocatalytic activity of La2O3 nanoparticles, J. Indian Chem. Soc. 100 (2023) 100860.
[47] C. Gómez-Rodríguez, Y. Antonio-Zárate, J. Revuelta-Acosta, L.F. Verdeja, D. Fernández-González, J.F. López-Perales, E.A. Rodríguez-Castellanos, L. V. García-Quiñonez, G.A. Castillo-Rodríguez, Research and development of novel refractory of MgO doped with ZrO2 nanoparticles for copper slag resistance, Materials 14 (9) (2021) 2277.
[48] L. Renuka, K.S. Anantharaju, S.C. Sharma, H.P. Nagaswarupa, S.C. Prashantha, H. Nagabhushana, Y.S. Vidya, Hollow microspheres Mg-doped ZrO2 nanoparticles: green assisted synthesis and applications in photocatalysis and photoluminescence, J. Alloys Compd. 672 (2016) 609–622.
[49] P. Khajuria, R. Mahajan, S. Kumar, R. Prakash, R.J. Choudhary, D.M. Phase, Surface and spectral investigation of Sm3+ doped MgO-ZrO2 phosphor, Optik 216 (2020) 164909.
[50] S. Akshatha, S. Sreenivasa, L. Parashuram, V. Udaya Kumar, T.M. Chakrapani Rao, S. Kumar, M.S. Raghu, Solvothermal synthesis of nanoscale disc-like gadolinium doped magnesium zirconate for highly efficient photocatalytic degradation of rhodamine B in water, SN Appl. Sci. 2 (2020) 1–10.
[51] P. Sen, P. Bhattacharya, G. Mukherjee, J. Ganguly, B. Marik, D. Thapliyal, S. Verma, G.D. Verros, M.S. Chauhan, R.K. Arya, Advancements in doping strategies for enhanced photocatalysts and adsorbents in environmental remediation, Technologies 11 (5) (2023) 144.
[52] K.C. Suresh, S. Surendhiran, P. Manoj Kumar, E. Ranjth Kumar, Y.A.S. Khadar, A. Balamurugan, Green synthesis of SnO2 nanoparticles using Delonix elata leaf extract: evaluation of its structural, optical, morphological and photocatalytic properties, SN Appl. Sci. 2 (2020), https://doi.org/10.1007/s42452-020-03534-z.
[53] J. Pachiyappan, N. Gnanansundaram, S. Sivamani, N.P.B.P. Sankari, N. Senthilnathan, G.A. Kerga, Preparation and characterization of magnesium oxide nanoparticles and its application for photocatalytic removal of rhodamine B and methylene blue dyes, J. Nanomater. 2022 (1) (2022) 6484573.
[54] R.H. Saadabadi, F.S. Tehrani, Z. Sabouri, M. Darroudi, Photocatalytic activity and anticancer properties of green synthesized ZnO-MgO-Mn2O3 nanocomposite via Ocimum basilicum L. seed extract, Sci. Rep. 14 (2024) 29812.
[55] G. Nasir, F. Batool, S. Noreen, H.Y. Gondal, M. Mustaqeem, Z. Saeed, Y. Gul, F. Ur Rehman, H.M. Ali, Biosynthesis of calcium oxide nanoparticles by employing Mulberry (Morus nigra) leaf extract as an efficient source for Rhodamine B remediation, Sci. Rep. 14 (1) (2024) 23744.
[56] S.A. Korde, P.B. Thombre, J.N. Sangshetti, A.S. Rajbhoj, S.T. Gaikwad, Green synthesis of binary nanostructured TiO2-ZrO2 composites using moringa oleifera gum: photocatalytic and antimicrobial applications, J. Mol. Struct. 1323 (2025) 140725.
[57] S. Haq, H. Afsar, M.B. Ali, M. Almalki, B. Albogami, A. Hedfi, Green synthesis and characterization of a ZnO-ZrO2 heterojunction for environmental and biological applications, Crystals 11 (12) (2021) 1502.
[58] S. Haq, A.W. Raja, S.U. Rehman, M.U. Sadiq, A.A. Alsaiari, J. Razzokov, F. Gulzar, Solar light-induced degradation of hazardous organic pollutants using Diospyros kaki mediated green synthesized zirconium doped nickel oxide-zinc oxide nanocomposite, Mater. Res. Express 11 (10) (2024) 105006.
[59] P.S. Sundara Selvam, D. Ganesan, V. Rajangam, A. Raji, V. Kandan, Green synthesis of SnO 2 nanoparticles for catalytic degradation of rhodamine B, Iran. J. Sci. Technol. Trans. A-Science 44 (2020) 661–676.
[60] S. Haq, H. Afsar, I.U. Din, P. Ahmad, M.U. Khandaker, H. Osman, S. Alamri, M. I. Shahzad, N. Shahzad, W. Rehman, M. Waseem, Enhanced photocatalytic activity of ficus elastica mediated zinc oxide-zirconium dioxide nanocatalyst at elevated calcination temperature: physicochemical study, Catalysts 11 (12) (2021) 1481.
[61] V. Devabharathi, K.S.G. Jagan, S.R. Priyan, T.M.N. Vidaarth, S. Surendhiran, Y.A. S. Khadar, K. Kandasamy, Rational design of NiO nanoflakes and porous GCN nanocomposite for synergic effectiveness on photocatalytic degradation of industry effluents and biological activity, Chem. Phys. Impact 8 (2024) 100637.
[62] B. Murugesan, D. Madhan, V. Devabharathi, D. Senthil Kumar, T. Aruna Christy, S. Surendhiran, A. Balamurugan, Y.A. Syed Khadar, Phytofabrication of MgO NPs wrapped on exfoliated g-C3N4 for antioxidant, antimicrobial degradation of toxic contaminants in water bodies, Inorg. Chem. Commun. 170 (2024) 113427.
[63] P. Nikolic, P. Mudgil, The cell wall, cell membrane and virulence factors of staphylococcus aureus and their role in antibiotic resistance, Microorganisms 11 (2023), https://doi.org/10.3390/microorganisms11020259.
[64] J. Zhang, P. Su, H. Chen, M. Qiao, B. Yang, X. Zhao, Impact of reactive oxygen species on cell activity and structural integrity of Gram-positive and Gram-negative bacteria in electrochemical disinfection system, Chem. Eng. J. 451 (2023) 138879, https://doi.org/10.1016/j.cej.2022.138879.